Contents lists available at ScienceDirect

Engineering

journal homepage: www.elsevier.com/locate/eng

Research
Material Science and Engineering—Article

A Nitride-Reinforced NbMoTaWHfN Refractory High-Entropy Alloy with Potential Ultra-High-Temperature Engineering Applications

Yixing Wan [a], Yanhai Cheng [a,*], Yongxiong Chen [b], Zhibin Zhang [b], Yanan Liu [a], Haijun Gong [a], Baolong Shen [c,*], Xiubing Liang [b,*]

[a] School of Mechanical and Electrical Engineering, China University of Mining and Technology, Xuzhou 221116, China
[b] Defense Innovation Institute, Academy of Military Science, Beijing 100071, China
[c] School of Materials Science and Engineering, Southeast University, Nanjing 211189, China

ARTICLE INFO

ABSTRACT

Refractory high-entropy alloys (RHEAs) have promising applications as the new generation of high-temperature alloys in hypersonic vehicles, aero-engines, gas turbines, and nuclear power plants. This study focuses on the microstructures and mechanical properties of the NbMoTaW(HfN)$_x$ ($x =$ 0, 0.3, 0.7, and 1.0) RHEAs. The alloys consist of multiple phases of body-centered cubic (BCC), hafnium nitride (HfN), or multicomponent nitride (MN) phases. As the x contents increase, the grain size becomes smaller, and the strength gradually increases. The compressive yield strengths of the NbMoTaWHfN RHEA at ambient temperature, 1000, 1400, and 1800 °C were found to be 1682, 1192, 792, and 288 MPa, respectively. The high-temperature strength of this alloy is an inspiring result that exceeds the high temperature and strength of most known alloys, including high-entropy alloys, refractory metals, and superalloys. The HfN phase has a significant effect on strengthening due to its high structural stability and sluggish grain coarsening, even at ultra-high temperatures. Its superior properties endow the NbMoTaWHfN RHEA with potential for a wide range of engineering applications at ultra-high temperatures. This work offers a strategy for the design of high-temperature alloys and proposes an ultra-high-temperature alloy with potential for future engineering applications.

© 2023 THE AUTHORS. Published by Elsevier LTD on behalf of Chinese Academy of Engineering and Higher Education Press Limited Company. This is an open access article under the CC BY-NC-ND license (http://creativecommons.org/licenses/by-nc-nd/4.0/).

1. Introduction

A new generation of refractory alloys with excellent high-temperature performance is urgently demanded for hypersonic vehicles, aero-engines, gas turbines, and nuclear power plants [1–4]. As the technology of these devices develops, the service temperature of their hot-ends is reaching 1800 °C or even higher (i.e., ultra-high temperatures) [5,6]. Traditional superalloys can hardly serve at such temperatures without additional physical cooling methods due to their low melting temperatures, all of which are no higher than 1300 °C [7–9]. Conventional solid-solution alloys, such as tungsten (W)-, tantalum (Ta)-, and molybdenum (Mo)-based single-principal-element alloys, exhibit insufficient strengths under such circumstances, due to their diffusion-dominated softening [10]. Mainly composed of refractory metal

elements, refractory high-entropy alloys (RHEAs) exhibit enhanced strength at temperatures above 1200 °C [11], causing them to attract a great deal of attention since 2010 [12–17]. For example, NbMoTaW and NbMoTaVW exhibit ultimate compressive strengths of 405 and 479 MPa at 1600 °C, respectively [13]. However, both NbMoTaW and NbMoTaVW RHEAs are intrinsically brittle at room temperature. Thus, it is essential to develop new alloys with improved ductility and enhanced high-temperature strength for engineering applications.

Recently, some instructive work has been done to overcome these issues. Han et al. [18,19] studied a TiNbMoTaW alloy and achieved a compressive strength (σ_m) of 814 MPa at 1200 °C by means of the solid-solution hardening effect. Wan et al. [20] prepared a ReMoTaW RHEA that achieved a compressive strength of 244 MPa at 1600 °C by reducing the lattice distortion and increasing the melting point. A NbMoTaWHf RHEA displayed a compressive strength of 232 MPa at 1600 °C with a high estimated melting point [21], while a NbMoTaWSi$_{0.25}$ RHEA was reported to have a compressive strength of 1071 MPa at 1200 °C, enhanced

by the second phase effect [22]. As the field developed further, the effect of ceramic secondary phases on the mechanical and microstructure of alloys was discovered. A $Mo_{0.5}NbHf_{0.5}ZrTiC_{0.3}$ RHEA was developed and found to be reinforced by MC-carbide particulates [23]. Wan et al. [24] fabricated $(NbMoTaW)_{100-x}C_x$ alloys, which were strengthened by face-centered cubic (FCC) structural carbides. Among these alloys, the compressive strength of a NbMoTaWC RHEA was reported to be about 2706 MPa at ambient conditions. By adjusting the carbon content, the plasticity and strength of NbMoTaW were simultaneously enhanced. Additional efforts were made to promote high-temperature strength. A $C_{0.25}Hf_{0.25}NbTaW_{0.5}$ RHEA exhibited a compressive yield strength of 749 MPa at 1400 °C [1], with carbides contributing to the alloy's high-temperature performance stability. The high-entropy alloy (HEA) matrix composites $Re_{0.5}MoNbW(TaC)_x$ showed enhanced strength at 1200 °C [4,25].

Moreover, some studies have demonstrated the effect of nitrogen (N) contents on the microstructures and mechanical properties of RHEAs. Wang et al. [26] achieved a high ultimate tensile strength of 1334 MPa and a ductility of 18.8% at ambient conditions in a $(TiZrNbTa)_{99.4}N_{0.6}$ RHEA. Lei et al. [27] discovered the strengthening effect of 2.0 atom percent (at%) nitrogen on a TiZrHfNb alloy. The tensile yield strength of the $(TiZrHfNb)_{98}N_2$ alloy was about 1300 MPa at ambient conditions. Unfortunately, little has been reported about alloys showing promising engineering application strengths at 1800 °C or above thus far.

Considering the high-temperature strength of the NbMoTaWHf RHEA and the excellent thermal stability of nitrides, the secondary strengthening of nitrides on a NbMoTaWHf base alloy seems to be an efficient approach to realize the "win–win" situation of high temperature and high strength at ultra-high temperatures. In the present study, $NbMoTaW(HfN)_x$ ($x = 0$, 0.3, 0.7, 1.0) RHEAs were designed and fabricated, and their microstructures, phases, and mechanical properties were investigated at room and elevated temperatures. The NbMoTaWHfN RHEA exhibited an inspiring result exceeding the application temperature and strength of most known alloys, including HEAs, refractory metals, and superalloys, and its phase formation and strengthening mechanism are discussed herein. Its superior properties endow the NbMoTaWHfN RHEA with potential for a wide range of engineering applications at ultra-high temperatures. This work offers a strategy for the design of high-temperature alloys and demonstrates the need for ultra-high-temperature alloys in engineering applications.

2. Material and methods

Alloy ingots with the nominal compositions of $NbMoTaW(HfN)_x$ ($x = 0$, 0.3, 0.7, 1.0) (henceforth referred to as NbMoTaW, $(HfN)_{0.3}$, $(HfN)_{0.7}$, and NbMoTaWHfN, respectively) were prepared by arc melting in a titanium (Ti)-gettered argon atmosphere. In order to avoid the interference of the raw materials in the investigation, the constituent element N was added from tantalum nitride (TaN). The purities of the raw materials were higher than 99.9 weight percent (wt%). The as-prepared ingots, each with a mass of 35 g, were flipped and remelted five times to ensure chemical homogeneity.

The crystal structures were identified by means of X-ray diffraction (XRD; D8 Advance, Bruker, Germany) with Cu Kα radiation and a 2θ range of 20°–90°. The microstructures were investigated with a scanning electron microscope (SEM; SU3500, HITACHI, Japan) equipped with a backscattered electron (BSE) detector. The phase distributions were determined by means of electron backscatter diffraction (EBSD) using an FEI Quanta 200 FEG SEM (the Netherlands). Before EBSD characterization, the samples were polished using 3 μm diamond paste and then polished using a

60 nm SiO_2 particle suspension. The alloys' chemical compositions were analyzed using an electron probe microanalyzer (EPMA; 8060G, SHIMADZU, Japan) with a wavelength dispersive spectrometer (WDS). The microstructures and selected area electron diffraction (SAED) patterns were analyzed using a field emission transmission electron microscope (TEM; G2 F20, FEI) equipped with an energy dispersive spectrometry (EDS) detector with an acceleration voltage of 200 kV. Room-temperature compression tests were conducted using an Instron 5982 (USA) testing machine with extensometers at a constant strain rate of 0.001 s^{-1} in air. The cylindrical specimens used for the compression tests were 5.4 mm in height and 3.6 mm in diameter. High-temperature compression tests were carried out using a high-temperature mechanical-properties testing machine (KAPPA 100, Zwick, Germany) in an argon atmosphere at 1000, 1400, and 1800 °C, respectively. The samples were heated to the target temperature at a rate of 10 °C·min^{-1}, kept at the target temperature for 10 min before the test, compressed with a 30% height reduction at a constant strain rate of 0.001 s^{-1}, and then furnace cooled (at a cooling rate of about 5 °C·min^{-1}). The annealed specimens were heated to the target temperature at a rate of 10 °C·min^{-1}, kept at the target temperature for 10 min, and then furnace cooled in a vacuum graphite furnace (VHT-2, Jinyan New Material Preparation Technology Co., Ltd., China).

3. Results

3.1. Analysis of the as-cast NbMoTaW(HfN)$_x$ (x = 0, 0.3, 0.7, and 1.0)

The XRD patterns of the as-cast $NbMoTaW(HfN)_x$ RHEAs are presented in Fig. 1(a). The $(HfN)_{0.7}$ and NbMoTaWHfN RHEAs showed a mixture of a dominant body-centered cubic (BCC) phase, secondary hafnium nitride (HfN) phase (FCC structure), and slight multicomponent nitride (MN) phase (a hexagonal close-packed (HCP) structure, where M represents the elements niobium (Nb), Mo, Ta, W, and Hf). The MN phase may be an MN with an HCP structure such as niobium nitride (NbN) and molybdenum nitride (MoN). The $(HfN)_{0.3}$ RHEA exhibited dominant BCC and secondary HfN phases. However, the NbMoTaW RHEA consisted of only a single BCC phase. As x increased, HfN and MN phases formed. As described in the Section 2, the element N was added in the form of TaN ceramic. Thus, the formation of the HfN and MN phases occurred during the solidification process, which may be a result of the tendency of nitrogen to bind to the metals in the alloy. This mechanism will be discussed in Section 4.1. As shown in Fig. 1(b), the peak position declined with the increase of x. The BCC phase's lattice constant in NbMoTaWHfN was about 3.255 Å (0.3255 nm), whereas that in NbMoTaW was 3.230 Å (0.323 nm). The dissolving Hf and N affected the composition of the BCC phase.

Figs. 2(a)–(d) shows the microstructures of the as-cast $NbMoTaW(HfN)_x$ RHEAs. Figs. 2(e)–(g) are the enlarged figures of each alloy. All the $NbMoTaW(HfN)_x$ RHEAs possessed dendritic structures. Their grain sizes are shown for reference (Fig. S1 in Appendix A). The grain sizes of BCC phase in $NbMoTaW(HfN)_x$ ($x = 0$, 0.3, 0.7, and 1.0) are 118.0, 16.2, 6.8, and 5.5 μm, respectively. Those of the nitride phase in $NbMoTaW(HfN)_x$ ($x = 0.3$, 0.7, and 1.0) are 5.30, 3.10, and 0.99 μm, respectively. As shown in Fig. 2(a), the NbMoTaW alloy (i.e., $x = 0$) showed only one phase, which was the BCC phase, judging from the XRD results. The $(HfN)_{0.3}$ alloy showed two contrast regions: bright and dark (Fig. 2(e)). Considering the XRD results of the $(HfN)_{0.3}$, the bright regions can be interpreted as the BCC phase, and the dark regions can be interpreted as the HfN phase. The $(HfN)_{0.7}$ alloy exhibited three regions: white, bright, and dark regions (Fig. 2(f)), which was consistent with the XRD results. The bright regions can be
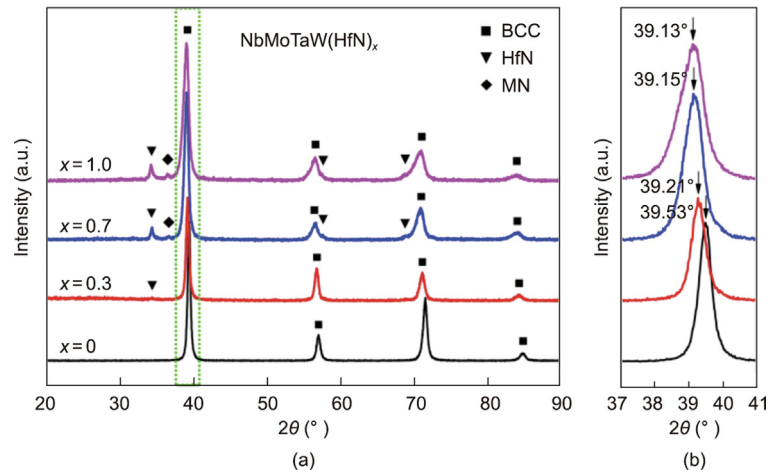
Fig. 1. (a) XRD patterns of the as-cast NbMoTaW(HfN)$_x$; (b) enlargement of each pattern in (a). BCC: body-centered cubic; MN: multicomponent nitride.
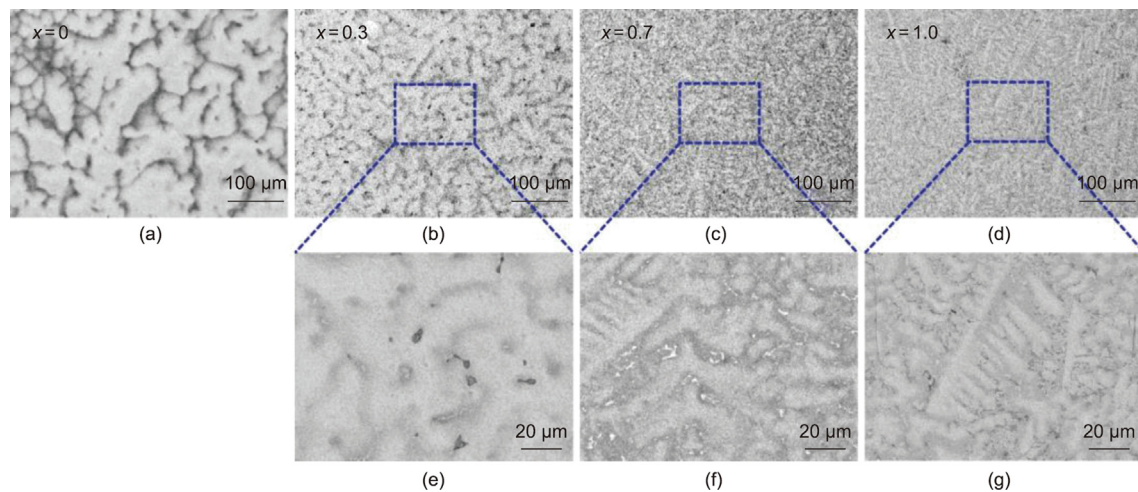

Fig. 2. (a–d) SEM images of the as-cast NbMoTaW(HfN)$_x$ under BSE mode: (a) $x=0$; (b) $x=0.3$; (c) $x=0.7$; and (d) $x=1.0$. (e–g) Enlarged figures of (b)–(d).

interpreted as the BCC phase, and the white and dark regions can be interpreted as the MN or HfN phases. As for the NbMoTaWHfN alloy (i.e., $x=1$), three phases should have been found, according to the XRD results. However, it was difficult to distinguish the HfN and MN phases by means of SEM under BSE mode, due to the small grain size of the dark regions. Thus, only two contrast regions are shown in Fig. 2(g). To facilitate the statistics of the grain sizes, the HfN and MN phases were measured as a whole phase, referred to as the nitride phase. As x increased, the grain size became smaller. For the BCC phase, the grain size decreased from 118.0 μm in NbMoTaW to 5.5 μm in NbMoTaWHfN. For the nitride phase, it decreased from 5.30 μm in (HfN)$_{0.3}$ to 0.99 μm in NbMoTaWHfN. For all the alloys, the BCC phase acted as the matrix, while the nitride phase acted as a dispersed phase distributed in the matrix.

Fig. 3 shows the compressive engineering stress–strain curves of the NbMoTaW(HfN)$_x$ at room temperature. The results are listed in Table 1. All the alloys with nitrides exhibited improved ductility compared with NbMoTaW. As x increased, the strength gradually increased, while the ductility decreased inversely. The yield strength ($\sigma_{0.2}$) and compressive strength (σ_m) of NbMoTaWHfN were 1682 and 2022 MPa, respectively, while those of NbMoTaW were only 1042 and 1059 MPa, respectively. The compressive strength of NbMoTaWHfN was about 1.9 times greater than that of the NbMoTaW RHEA, indicating the prominent strengthening effect of the nitride phase.
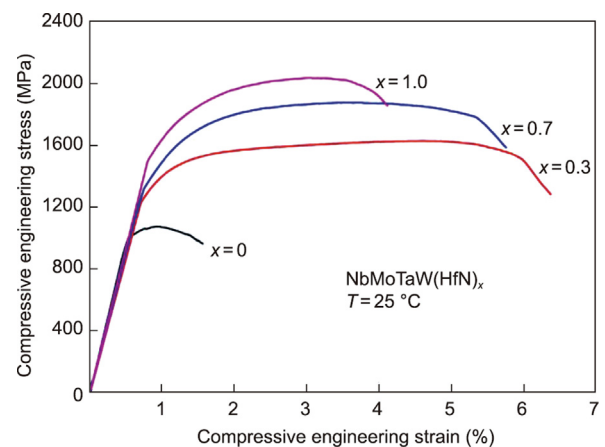

Fig. 3. Compressive engineering stress–strain curves of NbMoTaW(HfN)$_x$ at ambient conditions.

3.2. Characterizations of the as-cast NbMoTaWHfN RHEA

As the NbMoTaWHfN RHEA possessed the typical microstructures and highest compressive strength of the NbMoTaW(HfN)$_x$

Table 1

Yield strength ($\sigma_{0.2}$), compressive strength (σ_m), and fracture strain (ε) of NbMoTaW(HfN)$_x$ at different temperatures.

Alloy	Testing temperature (°C)	$\sigma_{0.2}$ (MPa)	σ_m (MPa)	ε (%)
NbMoTaW	25	1042	1059	0.9
(HfN)$_{0.3}$	25	1354	1616	4.8
(HfN)$_{0.7}$	25	1491	1863	3.9
NbMoTaWHfN	25	1682	2022	3.3
NbMoTaWHfN	1000	1192	2226	>30.0
NbMoTaWHfN	1400	792	860	>30.0
NbMoTaWHfN	1800	288	316	>30.0

Table 2

Chemical compositions (at%) of the as-cast NbMoTaWHfN.

Element	Bright region (BCC)	Dark region (nitride)
Nb	15.7	4.2
Mo	18.2	2.3
Ta	16.3	3.9
W	20.7	2.2
Hf	4.7	23.6
N	24.4	63.8

($x = 0$, 0.3, 0.7, and 1.0) RHEAs, it is necessary to clarify the microstructures of the as-cast NbMoTaWHfN RHEA in detail.

The phase distributions in NbMoTaWHfN obtained by means of EBSD analysis are displayed in Fig. 4. The red regions indicate the BCC phase, which occupies most of the area. The green regions are the FCC phase (here, this is HfN), which looks like an island chain. The yellow regions are the HCP phase (here, this is MN). The BCC phase acts as the matrix, the HfN phase acts as a subordinate phase distributed in the matrix, and the MN phase acts as a trace phase distributed around the HfN phase.

The distribution of the elements was revealed using the EPMA method (Fig. 5). The chemical compositions are exhibited in Table 2. The bright region was found to be enriched with Nb, Mo, Ta, and W, lacking Hf. Considering the random measurement error of the N, the bright region was determined to be the BCC structural

HEA dissolving the N. The dark region was found to be enriched in Hf and N; Nb, Mo, Ta, and W were also found in the dark regions. Thus, the dark region may be a mixing of the HfN and MN phases, which is consistent with the SEM analysis.

The microstructures and crystallographic structures of the as-cast NbMoTaWHfN RHEA were characterized by means of TEM (Fig. 6). Region A appears in the shape of a lath (with a grain size of ∼500 nm) with twins inside (circled in green). Region B acts as a matrix, with wavy dislocations inside. Region C also displays the shape of a lath (with a grain size of ∼1000 nm), with no dislocations or twins. As the SAED patterns show in Figs. 6(c)–(e), region A has an FCC phase crystalline structure (zone axis [101]), region B has a BCC phase crystalline structure (zone axis [001]), and region C has an HCP phase crystalline structure (zone axis [$11\bar{2}0$]). Fig. 6(f) shows a high-resolution TEM (HRTEM) image of the green region in Fig. 6(a) to clarify the structure. The FCC phase contains a high density of twins, which may be generated by excessive internal stress. During the phase formation stage, the formed FCC phase grains were squeezed by the neighboring formed BCC phase grains, which induced a local stress concentration in the formed FCC phase grains. The twins appeared when the local stress was higher than the critical shear stress. Meanwhile, the formed BCC phase grains were also compressed by the formed FCC phase grains. The compressive stress induced dislocations in the BCC phase near the phase boundaries. Fig. 6(g) shows an HRTEM image of the blue region in Fig. 6(b) to display the interface between the BCC and HCP phases. Misfit dislocations can be found in the interface, which can tolerate the lattice mismatch in different grains. The chemical compositions of the BCC, FCC, and HCP phases were examined by means of EDS (Fig. 6(h)). The FCC and HCP phases were found to enriched with Hf. The TEM results are consistent with the previous analysis.
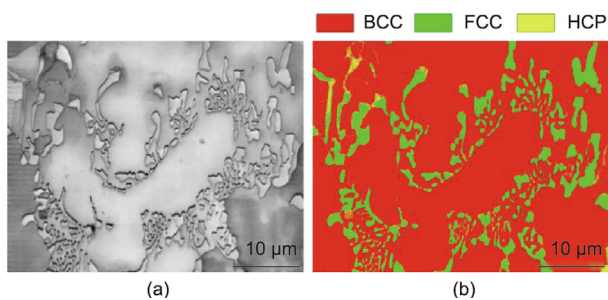

Fig. 4. (a) Image quality (IQ) map and (b) corresponding EBSD phase map of the as-cast NbMoTaWHfN.
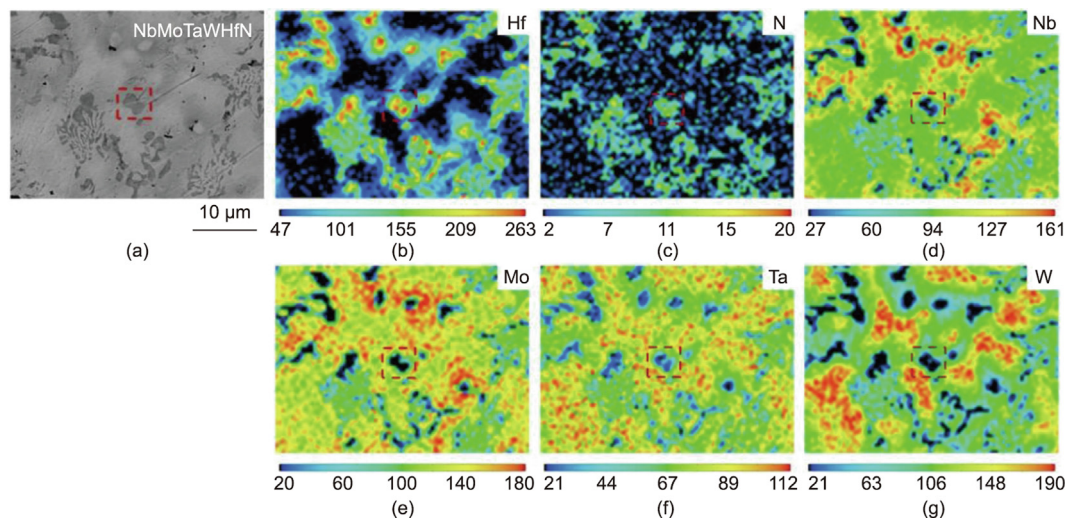

Fig. 5. (a) BSE image and (b–g) the corresponding EPMA element mappings of the as-cast NbMoTaWHfN.
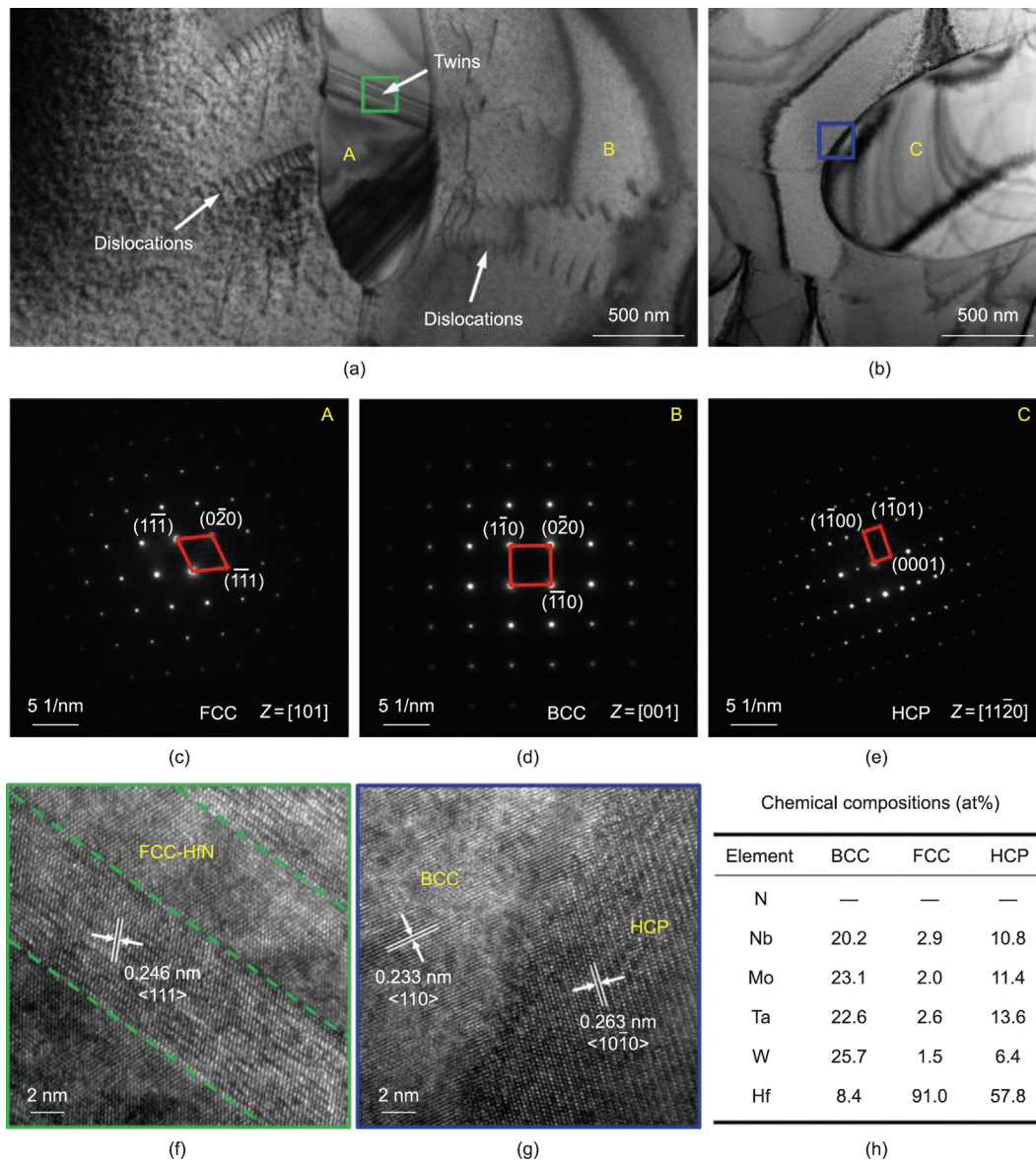
Fig. 6. Crystallographic structure of the as-cast NbMoTaWHfN. (a, b) Bright-field TEM images; (c–e) SAED patterns of the regions A, B, and C in (a) and (b); (f, g) high-resolution TEM (HRTEM) images of the green and blue regions in (a) and (b); (h) chemical compositions of the BCC, FCC, and HCP phases detected by EDS.

3.3. High-temperature properties of NbMoTaWHfN

Fig. 7(a) displays the compressive engineering stress–strain curves of NbMoTaWHfN at 1000, 1400, and 1800 °C. The corresponding results are listed in Table 1. As opposed to the situation at room temperature, the NbMoTaWHfN RHEA exhibited plastic deformation behavior above 1000 °C. At 1000 °C, the NbMoTaWHfN showed continuous strengthening with no peak stress until the final testing point at a strain of 30%. The alloy was enhanced by the work hardening effect, while the plasticity was improved through high-temperature dynamic softening. At 1400 and 1800 °C, the alloy exhibited peak stress at strains of about 5.5% and 3.7%, respectively. The yield strengths of NbMoTaWHfN at 1000, 1400, and 1800 °C were 1192, 792, and 288 MPa, respectively. Fig. 7(b) shows the enlarged curve at 1800 °C in Fig. 7(a) to exhibit the compressive properties clearly, and the inset shows the samples before and after compression at 1800 °C. The diameter of the sample increased from about 3.6 to 4.3 mm after compression at 1800 °C, with no cracks on the

sample surface. The compressive strength of the NbMoTaWHfN RHEA at 1800 °C was 316 MPa. Fig. 7(c) shows the yield stress of NbMoTaWHfN and other refractory alloys at different temperatures. It can be seen that most of the alloys have no data reported above 1600 °C [1,8,10,11,28,29], except for traditional refractory metals such as tantalum alloys and tungsten alloys, whereas the NbMoTaWHfN RHEA exhibited usable value strength even at 1800 °C, making it a potential structure alloy at that temperature. The NbMoTaWHfN RHEA showed an inspiring result exceeding the high temperature and strength of most known alloys, including HEAs, refractory metals, and superalloys. Moreover, the yield strengths of this alloy at temperatures between 1000 and 1800 °C were higher than those of other reported alloys, demonstrating its potential for prospective applications at different high temperatures.

Fig. 8(a) shows the XRD pattern of the NbMoTaWHfN RHEA after compression at 1800 °C; the XRD pattern of the as-cast RHEA and that of the RHEA after annealing at 1800 °C are also provided for reference. The NbMoTaWHfN RHEA was composed of BCC and
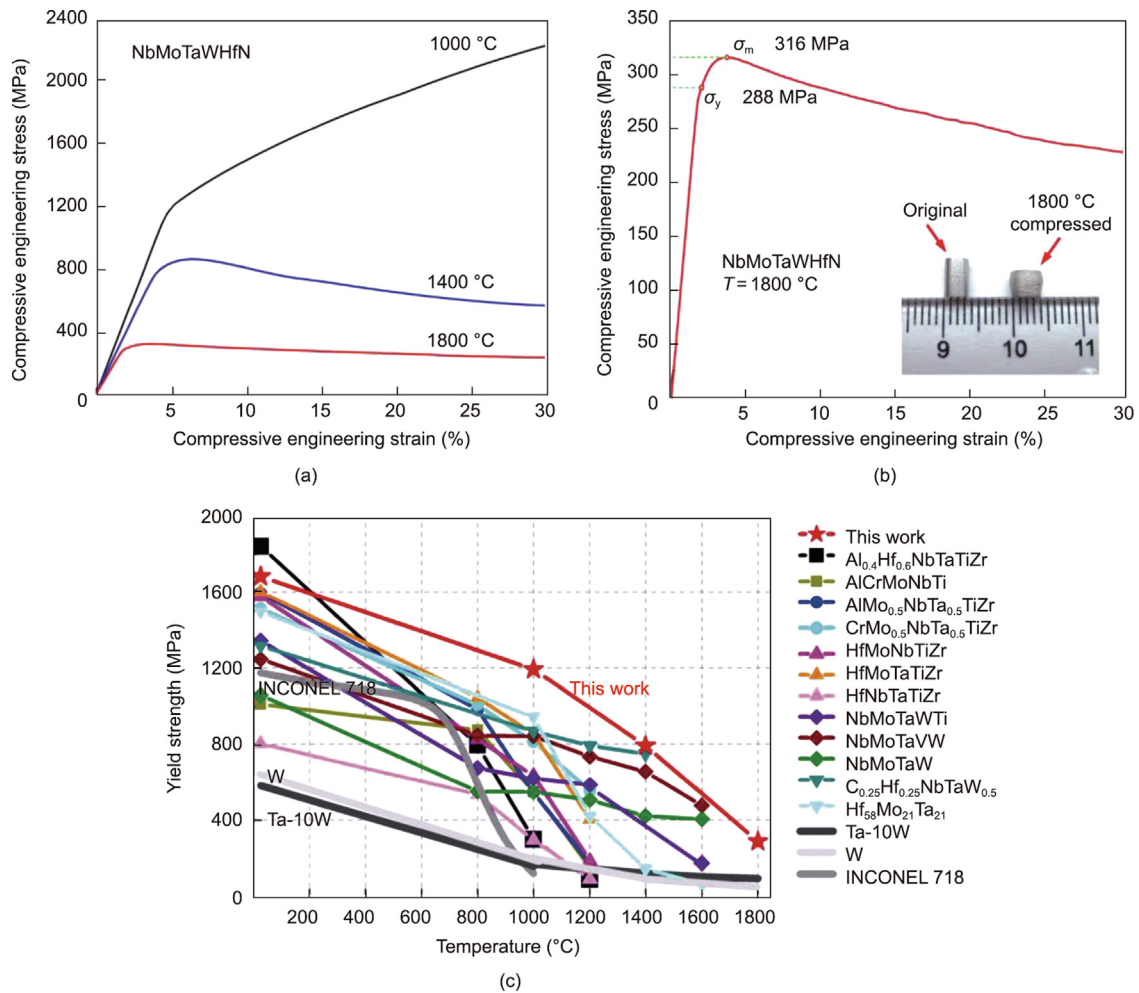
Fig. 7. (a) Compressive engineering stress–strain curves of NbMoTaWHfN at 1000, 1400, and 1800 °C; (b) enlarged curve for 1800 °C in (a); (c) yield stress of NbMoTaWHfN and other refractory alloys at different temperatures. σ_y: yield stress.
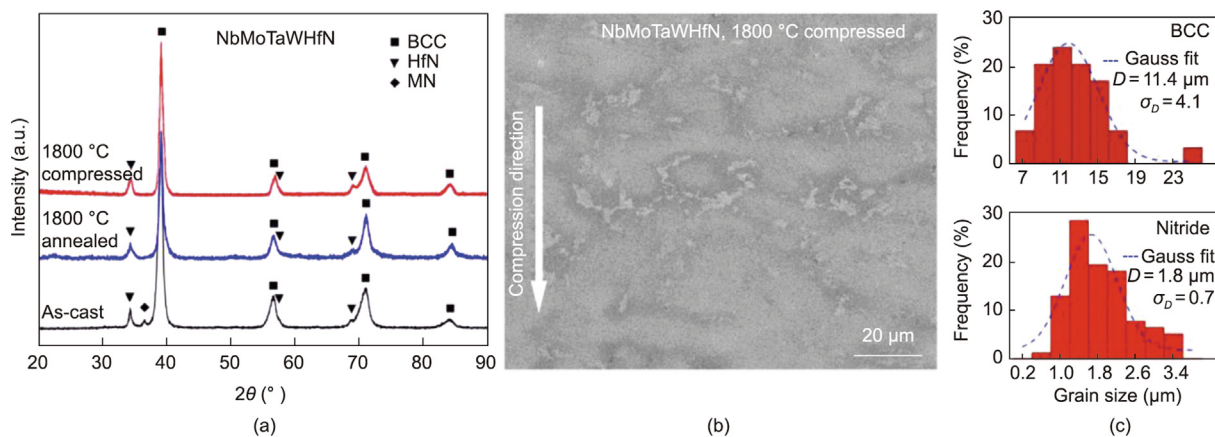

Fig. 8. (a) XRD pattern, (b) BSE image, and (c) grain-size distributions of the NbMoTaWHfN RHEA after compression at 1800 °C. D is the average grain size; σ_D is the standard deviation of the grain sizes.

HfN phases regardless of compression or annealing at 1800 °C. The BCC and HfN phases exhibited strong structural stability at 1800 °C. However, the diffraction peak at about 37° disappeared after compression, indicating dissolution of the MN phase through thermal diffusion. The disappearance of the MN phase was only related to temperature. Figs. 8(b) and (c) shows the BSE image and grain-size distributions of a cross-section of NbMoTaWHfN after compression at 1800 °C. No microcracks are observed in the alloy, indicating that the alloy possesses excellent plastic properties at 1800 °C, even at 30% shape deformation. Compared with the as-cast alloy, the dendritic structures are no longer evident.

The HfN phase was the dispersoid in the BCC matrix. The BCC phase grains grew from 5.5 to 11.4 μm, and those of the nitride phase (here, only the HfN phase) grew from 0.99 to 1.80 μm.

Considering the slow heating and cooling rate, the grain coarsening was caused by the high temperature during the whole heating and cooling process. On the other hand, the HfN phase was enriched. This indicated that the elements diffused at high temperatures, driven by the tendency of positive and negative atoms to combine. The HCP structural MN phase decomposed first at that high temperature, and the corresponding elements were then absorbed by the HfN phase and BCC phase, which contributed to the grain coarsening of the HfN phase.

Even though the grains of NbMoTaWHfN coarsened at high temperatures, they were still relatively fine compared with those of the as-cast NbMoTaW. Considering the grain sizes of the previously reported NbMoTaW [13], NbMoTaWV [13], NbMoTaWTi [14], and WReTaMo [20] RHEAs, the formation of the nitride phase is effective in hindering rapid grain coarsening.

Fig. 9 shows a bright-field TEM image of NbMoTaWHfN compressed at 1800 °C and the corresponding SAED patterns. Region A has the FCC phase (zone axis [011]), while region B has the BCC phase (zone axis [110]). Compared with the as-cast alloy, only the FCC and BCC phases were found, and no evidence of the HCP phase was found in the NbMoTaWHfN RHEA after compression at 1800 °C. These results are consistent with the previous analysis.

4. Discussion

4.1. Phase formation

Because formation of the nitride phase is effective in hindering rapid grain coarsening, it is essential to discuss the formation mechanism of the HfN and MN phases. As described in the Section 2, the element N was added in the form of TaN ceramic. Thus, the HfN and MN phases formed during the solidification process, which could be explained by the tendency of N to bind to the other metals. Table 3 summarizes the enthalpies of mixing for atomic pairs among N, Nb, Mo, Hf, Ta, and W [30]. It is well known that the enthalpy of mixing is an expression of the affinity between ele-

ments [31]. If the absolute value of the negative mixing enthalpy is large, it is easier for atomic pairs to bond [32]. As can be seen, the enthalpies of mixing with negative values for the N–Nb, N–Mo, N–Hf, N–Ta, and N–W atomic pairs are greater than those of the metal–metal atomic pairs. Therefore, the existence of the element N promoted the formation of nitrides due to nitrogen's easy combination with the constituent metals. Thus, the MN phase formed (here, the M represents Nb, Mo, Ta, W, and Hf). The MN phase was found to be an MN with an HCP structure such as NbN and MoN. In contrast, with no N as a constituent element, the NbMoTaW alloy (i.e., $x = 0$) formed only a single BCC phase. It should be noted that the value of the negative mixing enthalpy of the N–Hf atomic pair is as large as 218 kJ·mol^{-1}. Therefore, the HfN phase forms prior to other nitrides during the solidification, leading to the high content of the HfN phase in the NbMoTaWHfN RHEA. The residual metal elements (i.e., the Nb, Mo, Ta, W, and some Hf) in the $(HfN)_{0.3}$, $(HfN)_{0.7}$, and NbMoTaWHfN RHEAs formed the BCC phase according to the high entropy effect. Moreover, the solidification process was so fast under the conditions of the water-cooled copper crucible arc melting that not all the N formed nitrides. Hence, some N dissolved in the BCC phase.

4.2. Strengthening mechanism of NbMoTaW(HfN)$_x$ at ambient temperature

Formation of the nitride phase has a significant effect on enhancing the NbMoTaW(HfN)$_x$ RHEAs. As discussed in Section 3.1, the volume fraction and compressive strength of the nitride phases rose as the x content increased. The strengthening mechanism of NbMoTaW(HfN)$_x$ at ambient temperature can mainly be ascribed to the combination of grain-boundary strengthening, second-phase strengthening, and solid-solution strengthening.

First, grain-size refinement is effective in strengthening alloys through the grain-boundary strengthening mechanism [33]. Fig. 10 shows the changes in the average grain size of the BCC
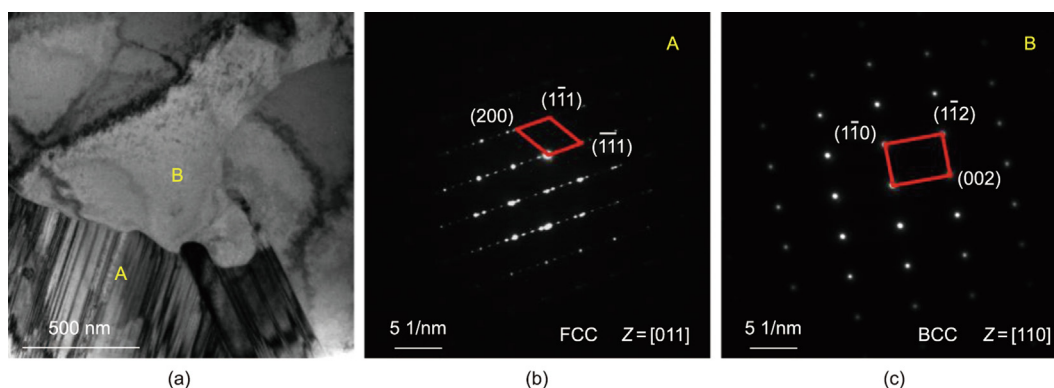

Fig. 9. (a) Bright-field TEM image of NbMoTaWHfN compressed at 1800 °C; (b, c) SAED patterns of the regions A and B in (a).

Table 3
Enthalpies of mixing between constituent elements (ΔH_{mix}, kJ·mol^{-1}) [30].

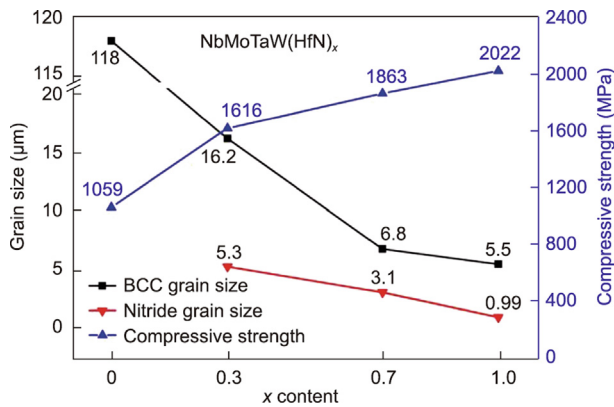| Element	ΔH_{mix} (kJ·mol^{-1})					
	N	Nb	Mo	Hf	Ta	W
N	—	−174	−115	−218	−173	−103
Nb	−174	—	−6	4	0	−8
Mo	−115	−6	—	−4	−5	0
Hf	−218	4	−4	—	3	−6
Ta	−173	0	−5	3	—	−7
W	−103	−8	0	−6	−7	—

Fig. 10. Grain-size distribution tendencies of the BCC and nitride phases in the as-cast NbMoTaW(HfN)$_x$. The compressive strength of each alloy is shown for reference.

and nitride phases for the NbMoTaW(HfN)$_x$ RHEAs. As the x content increases, the average grain sizes of the BCC and nitride phases continuously decrease. Meanwhile, the strengths of the alloys continuously increase. The average grain size of the BCC phase in NbMoTaWHfN was about 5.5 μm, which is smaller than that of NbMoTaW (∼118 μm). As is well known, the strength of alloys can be improved by refining the grains [34]. The relationship between the strength (σ) and grain size can be expressed by the Hall–Petch relationship [35,36]:

$$\sigma = \sigma_0 + K \cdot d^{-1/2} \tag{1}$$

where σ_0 is the lattice friction, K is the strengthening coefficient, and d is the grain diameter. Refining the grain means increasing the grain boundary, effectively impeding the propagation of dislocations from one grain to the neighbors, leading to dislocation pile-up in deformed grains.

Second, the homogeneously distributed nitrides interacted with the BCC phase, enhancing the alloys by means of second-phase strengthening. The average grain sizes of the nitrides in the (HfN)$_{0.3}$, (HfN)$_{0.7}$, and NbMoTaWHfN RHEAs were about 1–5 μm; in contrast, those of the BCC phase were 5–16 μm (Fig. 10). The Orowan mechanism is a dislocation bypass mechanism that occurs when the radius of particles exceeds a critical value or is incoherent with the matrix [37]. When a moving dislocation encounters a nitride particle, a dislocation ring will form, increasing the required external force, which provides the deformation force. The contribution of the precipitation strengthening can be measured by the grain boundary barrier stress. The relationship between the shear stress of the dislocation bypassing the second phase and the second phase can be expressed as follows:

$$\tau = Gb/\lambda \tag{2}$$

where τ is the shear stress of the dislocation bypassing the second phase, G is the modulus of shear elasticity, b is the value of the Burst vector, and λ is the distance of each second-phase particle. λ is directly proportional to the grain diameter d. Thus, the shear stress τ is inversely proportional to the mean precipitate radius d. The smaller d is, the more significant the strengthening effect.

Third, the large number of principal elements in the NbMoTaW(HfN)$_x$ RHEAs resulted in a large solid solution strengthening effect [38,39]. In the BCC phase, a large number of solute atoms gathered around dislocations, hindering the movement of dislocations. Furthermore, the element N, which has a small atomic radius, has a significant effect on solid-solution strengthening. The atomic radius of N is 0.74 Å (0.074 nm), while those of Nb, Mo, Hf, Ta, and W are 1.45 Å (0.145 nm), 1.45 Å (0.145 nm), 1.55 Å

(0.155 nm), 1.45 Å (0.145 nm), and 1.35 Å (0.135 nm), respectively [40]. The atomic radius of N is much smaller than those of the other constituent elements. Some N solubilized into the lattice of the BCC phase, forming an interstitial solid solution. The interstitial atoms may cause lattice distortion and change lattice constants. The lattice constants increase with the dissolution of solute atoms. Therefore, the interstitial N strengthened the NbMoTaW(HfN)$_x$ RHEAs.

4.3. Strengthening mechanism of the NbMoTaWHfN RHEA at elevated temperature

The NbMoTaWHfN RHEA exhibited an extremely high compressive strength of 316 MPa, even at 1800 °C. The strengthening mechanism of the NbMoTaWHfN RHEA at elevated temperatures should be clarified. Considering the high stability of the BCC and HfN phases at 1800 °C, the strengthening mechanism can be mainly ascribed to the combination of a high softening temperature, grain-boundary strengthening, and second-phase strengthening.

First, the high strength of NbMoTaWHfN at high temperatures is related to the high softening temperature. Generally speaking, the softening temperature for an alloy is approximately $0.6T_m$ [13,14] (where the melting temperature, T_m, is given in K). The T_m of the RHEAs can be calculated by the rule of mixtures [41]:

$$T_m = \sum_{i=1}^{n} c_i T_{mi} \tag{3}$$

where c_i is the atomic percentage of the ith component, and T_{mi} is the melting temperature of the ith component. Considering that the FCC and HCP phases were merely dispersed, they can be considered to make less of a contribution to the melting temperature. Therefore, the T_m of NbMoTaWHfN can be assessed by the BCC phase. Hence, the melting temperature of the NbMoTaWHfN RHEA can be estimated, as summarized in Table 4 with the corresponding metals and nitrides [40,42]. The calculated melting temperature of the NbMoTaWHfN RHEA is 3027 K (i.e., 2754 °C). So, the softening temperature of the NbMoTaWHfN RHEA is about 1816 K (1543 °C). In addition, the T_m of HfN is 3578 K, and the T_m of the other nitrides are higher than the softening temperature of the NbMoTaWHfN RHEA (except for the heat-induced decomposed WN). Thus, the nitrides would have no negative effect on the softening temperature if they were to be considered. The HfN phase has a significant effect on the high-temperature strength, due to its high structural stability and sluggish grain coarsening. Although the T_m of the NbMoTaWHfN RHEA is slightly lower compared with those of the NbMoTaW [13], NbMoTaWV [13], and WReTaMo [20] RHEAs, the NbMoTaWHfN RHEA still showed a high softening temperature, which appeared to have a significant effect on the elevated-temperature strength of NbMoTaWHfN. Furthermore, the structural stabilities of the BCC and HfN phases help to maintain

Table 4
T_m of NbMoTaWHfN, constituent elements, and corresponding nitrides.

Material	T_m (K)	Ref.
Nb	2750	[40]
Mo	2896	[40]
Ta	3290	[40]
W	3695	[40]
Hf	2506	[40]
NbN	2846	[42]
MoN	2023	[42]
TaN	3633	[42]
WN	Decomposes	[42]
HfN	3578	[42]
NbMoTaWHfN	3027	This work

the strength of the alloy. The high strength of NbMoTaWHfN at 1800 °C suggests the inspiring potential application of refractory alloys at ultra-high temperatures.

Second, the grain-boundary strengthening mechanism remains available for NbMoTaWHfN at high temperatures. As discussed above, the NbMoTaWHfN RHEA's average grain size increased after annealing at 1800 °C (Fig. 8). However, compared with that of the NbMoTaW RHEA, the grain size was still tiny. According to the Hall–Petch relationship (Eq. (1)), this kind of refined grain could strengthen the alloy even at 1800 °C. The capacity of the NbMoTaWHfN RHEA to maintain a low grain growth tendency is important for fine-grain strengthening at high temperatures.

Third, the structurally stable HfN phase strengthens the NbMoTaWHfN RHEA via second-phase strengthening. As shown in Fig. 8, the HfN phase's grain size was 1.8 µm, which is significantly smaller than the 11.4 µm grain of the BCC phase. The HfN phase with a stable structure at high temperature was still dispersed in the BCC matrix and strengthened the alloy in the form of the dispersion phase, even at 1800 °C. According to Eq. (2), the dislocation bypasses the dispersion phase producing shear stress. During deformation at high temperatures, the dislocation should bypass the dispersion particles and form dislocation rings, resulting in an increase in strength.

4.4. Superior mechanical properties and potential engineering applications

Fig. 11 shows the reported highest testing temperature and corresponding yield strength of various alloys. It can be seen that the highest testing temperature of most alloys is no more than 1600 °C. The highest testing temperature of 3d transition metal HEAs is 1100 °C [43–46]. Depending on the alloy component, the ultimate service temperature of an RHEA ranges from 1100 °C to about 1600 °C [3,11,47]. In order to meet the urgent demand for ultra-high temperature service alloys in the aerospace field, a new type of alloy called the ultra-high-temperature HEA (UHT-HEA) has been proposed, which can serve at temperatures greater than 1800 °C. The target is to design alloys with higher strength at higher temperatures. Unfortunately, little has been reported on UHT-HEAs so far. Except for this work, only the data for traditional refractory metals (e.g., tantalum alloys and tungsten alloys) have been reported within that temperature range. However, the strengths of these alloys are rather low at temperatures above 1800 °C. In this work, the NbMoTaWHfN RHEA is reported to exhibit a novel compressed $\sigma_{0.2}$ of 288 MPa and σ_m of 316 MPa at 1800 °C. The NbMoTaWHfN RHEA exhibits the highest strength in the ultra-high temperature region, classifying it as a UHT-HEA.

High-temperature structural materials have become key materials in the fields of national defense and civil industries, which are related to national interests. Fig. 12 displays some potential engineering applications for the NbMoTaWHfN RHEA. As shown in Fig. 12(a), the temperature of the turbine inlet for the fifth-generation aero-engine will reach 2000 °C [6,48]. As shown in Fig. 12(b), hypersonic vehicles, which are attracting a great deal of attention from the world's military powers, encounter drastic aerodynamic heating, rapid rises and drops in temperature, oxidation, mechanical stripping, and other extreme environments upon reentering the atmosphere, with a working temperature of 2200 °C
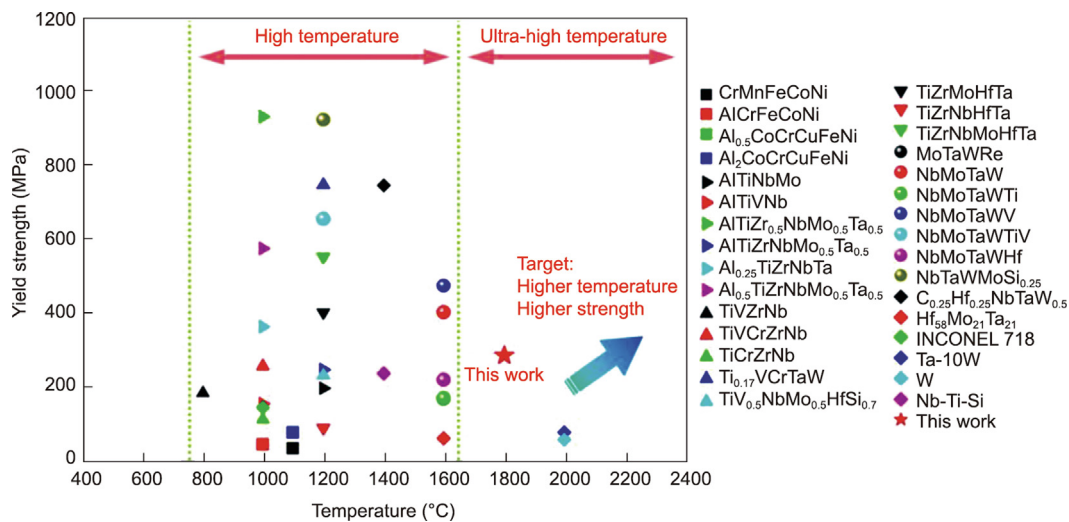

Fig. 11. The reported highest testing temperatures and corresponding yield strengths of various alloys.
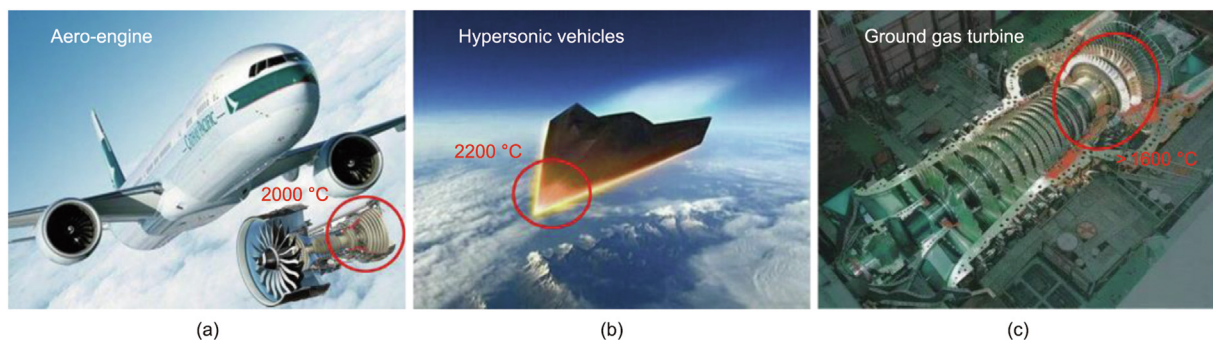

Fig. 12. Potential engineering applications for the NbMoTaWHfN RHEA. (a) Aero-engine, (b) hypersonic vehicles, and (c) ground gas turbine.

at the nose cone and the leading edge of the aircraft [6,49,50]. In civil industries, the temperature of the gas injected into the blade of a ground gas turbine exceeds 1600 °C (Fig. 12(c)) [51]. Currently, the alloys used in refractory industry fields are traditional superalloys (based on nickel, cobalt, or iron). However, these superalloys' intrinsic service temperature is no more than 1200 °C [49], at which they are already at 90% of their melting point [52]. The industrial fields of aviation, aerospace, weapons, and gas turbines are developing rapidly at present, with the continual emergence of new designs that increase the flying speed and thrust–weight ratio, resulting in more stringent requirements for high-temperature strength for the key structural materials. As technology develops, the traditional superalloys can hardly meet these stringent requirements, whether they be for a high service temperature or high-temperature strength. There is no time to waste in the development of alloys with advanced properties for ultra-high-temperature environments. Assessed with high-temperature strength, the NbMoTaWHfN RHEA can meet the stringent requirements mentioned above. Other potential engineering applications may include structural fire engineering, high-temperature cutting tools, and so forth.

5. Conclusions

In this work, NbMoTaW(HfN)$_x$ RHEAs were synthesized using vacuum arc melting. The high-temperature compressive properties and potential ultra-high-temperature engineering applications of the novel NbMoTaWHfN RHEA were studied in detail. Based on the experimental results and their analysis, the following main conclusions were drawn:

(1) The NbMoTaW(HfN)$_x$ RHEAs (x = 0.3, 0.7, and 1.0) exhibited multi-phase combinations of BCC, HfN, or MN phases. As the Hf and N contents increased, the grain size became smaller, and the strength gradually increased. All the alloys with nitrides exhibited improved ductility compared with NbMoTaW. The compressive yield strengths of the NbMoTaWHfN RHEA at ambient temperature, 1000, 1400, and 1800 °C were 1682, 1192, 792, and 288 MPa, respectively.

(2) The yield strengths of NbMoTaWHfN at temperatures between 1000 and 1800 °C were found to be higher than those of other reported alloys, indicating its potential for prospective applications at various high temperatures. The NbMoTaWHfN RHEA exhibited high strength even at 1800 °C, which was an inspiring result exceeding the high temperature and strength of most known alloys. The HfN phase has a significant effect on the alloy's high-temperature strength due to its high structural stability and sluggish grain coarsening.

(3) The phase formation and strengthening mechanism of the alloy were discussed. The strengthening mechanism of the NbMoTaWHfN RHEA at elevated temperatures was mainly ascribed to the combination of a high softening temperature, grain-boundary strengthening, and second-phase strengthening.

(4) Its superior properties endow the NbMoTaWHfN RHEA with potential for wide-ranging engineering applications at ultra-high temperatures.

Acknowledgments

Compliance with ethics guidelines

Yixing Wan, Yanhai Cheng, Yongxiong Chen, Zhibin Zhang, Yanan Liu, Haijun Gong, Baolong Shen, and Xiubing Liang declare that they have no conflict of interest or financial conflicts to disclose.

Appendix A. Supplementary data

Supplementary data to this article can be found online at https://doi.org/10.1016/j.eng.2023.06.008.

References

[1] Wu S, Qiao D, Zhang H, Miao J, Zhao H, Wang J, et al. Microstructure and mechanical properties of C$_x$Hf$_{0.25}$NbTaW$_{0.5}$ refractory high-entropy alloys at room and high temperatures. J Mater Sci Technol 2022;97:229–38.
[2] Wang Z, Wu H, Wu Y, Huang H, Zhu X, Zhang Y, et al. Solving oxygen embrittlement of refractory high-entropy alloy via grain boundary engineering. Mater Today 2022;54:83–9.
[3] Feng R, Feng B, Gao MC, Zhang C, Neuefeind JC, Poplawsky JD, et al. Superior high-temperature strength in a supersaturated refractory high-entropy alloy. Adv Mater 2021;33(48):2102401.
[4] Wei Q, Xu X, Shen Q, Luo G, Zhang J, Li J, et al. Metal-carbide eutectics with multiprincipal elements make superrefractory alloys. Sci Adv 2022;8(27): eabo2068.
[5] Uyanna O, Najafi H. Thermal protection systems for space vehicles: a review on technology development, current challenges and future prospects. Acta Astronaut 2020;176:341–56.
[6] Zhang S, Li X, Zuo J, Qin J, Cheng K, Feng Y, et al. Research progress on active thermal protection for hypersonic vehicles. Prog Aerosp Sci 2020;119:100646.
[7] Pineau A, Antolovich SD. High temperature fatigue of nickel-base superalloys—a review with special emphasis on deformation modes and oxidation. Eng Fail Anal 2009;16(8):2668–97.
[8] Miracle DB, Senkov ON. A critical review of high entropy alloys and related concepts. Acta Mater 2017;122:448–511.
[9] Wan ZP, Shen JY, Wang T, Wei K, Li Z, Yan S, et al. Effect of hot deformation parameters on the dissolution of γ′ precipitates for as-cast Ni-based superalloys. J Mater Eng Perform 2022;31(2):1594–606.
[10] Zhang X, Tian J, Xue M, Jiang F, Li S, Zhang B, et al. Ta–W refractory alloys with high strength at 2000 °C. Acta Metall Sin 2022;58(10):1253–60. Chinese.
[11] Couzinié JP, Senkov ON, Miracle DB, Dirras G. Comprehensive data compilation on the mechanical properties of refractory high-entropy alloys. Data Brief 2018;21:1622–41.
[12] Senkov ON, Wilks GB, Miracle DB, Chuang CP, Liaw PK. Refractory high-entropy alloys. Intermetallics 2010;18(9):1758–65.
[13] Senkov ON, Wilks GB, Scott JM, Miracle DB. Mechanical properties of Nb$_{25}$Mo$_{25}$Ta$_{25}$W$_{25}$ and V$_{20}$Nb$_{20}$Mo$_{20}$Ta$_{20}$W$_{20}$ refractory high entropy alloys. Intermetallics 2011;19(5):698–706.
[14] Wan Y, Mo J, Wang X, Zhang Z, Shen B, Liang X. Mechanical properties and phase stability of WTaMoNbTi refractory high-entropy alloy at elevated temperatures. Acta Metall Sin 2021;34(11):1585–90.
[15] Mo J, Wan Y, Zhang Z, Wang X, Li X, Shen B, et al. First-principle prediction of structural and mechanical properties in NbMoTaWRe$_x$ refractory high-entropy alloys with experimental validation. Rare Met 2022;41(10):3343–50.
[16] Senkov ON, Scott JM, Senkova SV, Meisenkothen F, Miracle DB, Woodward CF. Microstructure and elevated temperature properties of a refractory TaNbHfZrTi alloy. J Mater Sci 2012;47(9):4062–74.
[17] Guo NN, Wang L, Luo LS, Li XZ, Su YQ, Guo JJ, et al. Microstructure and mechanical properties of refractory MoNbHfZrTi high-entropy alloy. Mater Des 2015;81:87–94.
[18] Han ZD, Luan HW, Liu X, Chen N, Li XY, Shao Y, et al. Microstructures and mechanical properties of Ti$_x$NbMoTaW refractory high-entropy alloys. Mater Sci Eng A 2018;712:380–5.
[19] Han ZD, Chen N, Zhao SF, Fan LW, Yang GN, Shao Y, et al. Effect of Ti additions on mechanical properties of NbMoTaW and VNbMoTaW refractory high entropy alloys. Intermetallics 2017;84:153–7.
[20] Wan Y, Wang Q, Mo J, Zhang Z, Wang X, Liang X, et al. WReTaMo refractory high-entropy alloy with high strength at 1600 °C. Adv Eng Mater 2022;24(2):2100765.
[21] Wan Y. Study on the preparation and mechanical properties of rare metals Nb/Mo/Ta/W based ultra-high-temperature high-entropy alloys [dissertation]. Xuzhou: China University of Mining and Technology; 2021. Chinese.
[22] Guo Z, Zhang A, Han J, Meng J. Effect of Si additions on microstructure and mechanical properties of refractory NbTaWMo high-entropy alloys. J Mater Sci 2019;54(7):5844–51.
[23] Guo NN, Wang L, Luo LS, Li XZ, Chen RR, Su YQ, et al. Microstructure and mechanical properties of in-situ MC-carbide particulates-reinforced refractory Mo$_{0.5}$NbHf$_{0.5}$ZrTi matrix alloy composite. Intermetallics 2016;69:74–7.

[24] Wan Y, Wang X, Zhang Z, Mo J, Shen B, Liang X. Structures and properties of the (NbMoTaW)$_{100-x}$C$_x$ high-entropy composites. J Alloys Compd 2021;889:161645.

[25] Wei Q, Shen Q, Zhang J, Zhang Y, Luo G, Zhang L. Microstructure evolution, mechanical properties and strengthening mechanism of refractory high-entropy alloy matrix composites with addition of TaC. J Alloys Compd 2019;777:1168–75.

[26] Wang R, Tang Y, Lei Z, Ai Y, Tong Z, Li S, et al. Achieving high strength and ductility in nitrogen-doped refractory high-entropy alloys. Mater Des 2022;213:110356.

[27] Lei Z, Liu X, Wu Y, Wang H, Jiang S, Wang S, et al. Enhanced strength and ductility in a high-entropy alloy via ordered oxygen complexes. Nature 2018;563(7732):546–50.

[28] Wu M, Li S, Xu D, Zhao H. Mechanical properties of alloy Ta-10W at elevated temperature. Rare Met Mater Eng 2006;35(z1):64–7. Chinese.

[29] Senkov ON, Daboiku TI, Butler TM, Titus MS, Philips NR, Payton EJ. High-temperature mechanical properties and oxidation behavior of Hf-27Ta and Hf-21Ta-21X (X is Nb, Mo or W) alloys. Int J Refract Met Hard Mater 2021;96:105467.

[30] Takeuchi A, Inoue A. Classification of bulk metallic glasses by atomic size difference, heat of mixing and period of constituent elements and its application to characterization of the main alloying element. Mater Trans 2005;46(12):2817–29.

[31] Inoue A, Shen BL. A new Fe-based bulk glassy alloy with outstanding mechanical properties. Adv Mater 2004;16(23–24):2189–92.

[32] Ye YF, Wang Q, Lu J, Liu CT, Yang Y. High-entropy alloy: challenges and prospects. Mater Today 2016;19(6):349–62.

[33] Liu WH, Wu Y, He JY, Nieh TG, Lu ZP. Grain growth and the Hall–Petch relationship in a high-entropy FeCrNiCoMn alloy. Scr Mater 2013;68(7):526–9.

[34] Kang B, Lee J, Ryu HJ, Hong SH. Microstructure, mechanical property and Hall–Petch relationship of a light-weight refractory Al$_{0.1}$CrNbVMo high entropy alloy fabricated by powder metallurgical process. J Alloys Compd 2018;767:1012–21.

[35] Chen S, Tseng KK, Tong Y, Li W, Tsai CW, Yeh JW, et al. Grain growth and Hall–Petch relationship in a refractory HfNbTaZrTi high-entropy alloy. J Alloys Compd 2019;795:19–26.

[36] Lee C, Song G, Gao MC, Feng R, Chen P, Brechtl J, et al. Lattice distortion in a strong and ductile refractory high-entropy alloy. Acta Mater 2018;160:158–72.

[37] He JY, Wang H, Huang HL, Xu XD, Chen MW, Wu Y, et al. A precipitation-hardened high-entropy alloy with outstanding tensile properties. Acta Mater 2016;102:187–96.

[38] Zhang Y, Zhou YJ, Lin JP, Chen GL, Liaw PK. Solid-solution phase formation rules for multi-component alloys. Adv Eng Mater 2008;10(6):534–8.

[39] Senkov ON, Pilchak AL, Semiatin SL. Effect of cold deformation and annealing on the microstructure and tensile properties of a HfNbTaTiZr refractory high entropy alloy. Metall Mater Trans A 2018;49(7):2876–92.

[40] webelements.com [Internet]. Mark J Winter; c1993–2023 [cited 2023 Jan 16]. Available from: https://www.webelements.com/.

[41] Melnick AB, Soolshenko VK. Thermodynamic design of high-entropy refractory alloys. J Alloys Compd 2017;694:223–7.

[42] chemicalbook.com [Internet]. Beijing: ChemicalBook; c2016–2021 [cited 2023 Jan 16]. Available from: https://www.chemicalbook.com/. Chinese.

[43] Gorsse S, Nguyen MH, Senkov ON, Miracle DB. Database on the mechanical properties of high entropy alloys and complex concentrated alloys. Data Brief 2018;21:2664–78.

[44] George EP, Raabe D, Ritchie RO. High-entropy alloys. Nat Rev Mater 2019;4(8):515–34.

[45] Stepanov ND, Shaysultanov DG, Yurchenko NY, Zherebtsov SV, Ladygin AN, Salishchev GA, et al. High temperature deformation behavior and dynamic recrystallization in CoCrFeNiMn high entropy alloy. Mater Sci Eng A 2015;636:188–95.

[46] Praveen S, Kim HS. High-entropy alloys: potential candidates for high-temperature applications—an overview. Adv Eng Mater 2018;20(1):1700645.

[47] Chen J, Zhou X, Wang W, Liu B, Lv Y, Yang W, et al. A review on fundamental of high entropy alloys with promising high-temperature properties. J Alloys Compd 2018;760:15–30.

[48] Choubey G, Yuvarajan D, Huang W, Shafee A, Pandey KM. Recent research progress on transverse injection technique for scramjet applications—a brief review. Int J Hydrogen Energy 2020;45(51):27806–27.

[49] Ni D, Cheng Y, Zhang J, Liu JX, Zou J, Chen B, et al. Advances in ultra-high temperature ceramics, composites, and coatings. J Adv Ceram 2022;11(1):1–56.

[50] Le VT, Ha NS, Goo NS. Advanced sandwich structures for thermal protection systems in hypersonic vehicles: a review. Compos Part B Eng 2021;226:109301.

[51] González-Barrio H, Calleja-Ochoa A, Lamikiz A, López de Lacalle LN. Manufacturing processes of integral blade rotors for turbomachinery, processes and new approaches. Appl Sci 2020;10(9):3063.

[52] LeHolm R, Norris B, Gurney A. High temperature alloys for aerospace structures. Adv Mater Process 2001;159(5):27–31.